UMYU Scientifica, Vol. 5 NO. 1, March 2026, Pp 344 – 358
https://doi.org/10.56919/usci.2651.029
ISSN: 2955 – 1145 (print); 2955 – 1153 (online)
A periodical of the Faculty of Natural and Applied Sciences, UMYU, Katsina

ORIGINAL RESEARCH ARTICLE

Defect and Temperature Effects in $MASnI_3$ Perovskite Solar Cells: A SCAPS-1D Simulation Study with Interface and Recombination Analysis

Hassan Abdulsalam[1]* and Fatima Musa Lariski[1]

[1]Department of Physics, Yobe State University, P.M.B. 1144, Damaturu, Yobe State, Nigeria

ABSTRACT

Tin-based perovskite solar cells (PSCs), particularly methylammonium tin triiodide ($MASnI_3$), have emerged as promising lead-free alternatives to conventional lead-based devices. However, their performance is significantly limited by defect-induced recombination and thermal instability. In this work, a systematic SCAPS-1D simulation study is conducted to investigate the coupled effects of absorber thickness, bulk defect density, interface defect states, band alignment, and operating temperature on device performance. The simulation model is constructed using experimentally reported material parameters and benchmarked against literature-reported efficiency ranges (5–9%) to ensure physical relevance. Results indicate that an optimal absorber thickness of 600 nm yields a power conversion efficiency (PCE) of 17.31%, representing a balance between optical absorption and carrier transport. Bulk defect density is identified as the dominant performance-limiting factor, with PCE decreasing sharply from 25.05% to 4.47% as defect density increases from 10^9 to 10^{16} cm^{-3} due to enhanced Shockley–Read–Hall recombination. Interface analysis reveals that the $MASnI_3$/Spiro-OMeTAD junction is more sensitive to defect states than the TiO_2/$MASnI_3$ interface, leading to significant degradation in fill factor and current density at high trap densities. Band alignment optimization indicates that small positive offsets (0 to +0.20 eV) can suppress interfacial recombination while maintaining efficient charge extraction. Temperature-dependent analysis demonstrates performance improvement up to ~400 K, followed by degradation due to increased recombination and bandgap narrowing. Although the study is based on numerical simulation without direct experimental validation, the results are consistent with experimentally observed trends and provide semi-quantitative insights. The findings therefore offer practical design guidelines rather than absolute performance predictions, highlighting critical defect thresholds and interface engineering strategies for improving $MASnI_3$ solar cell performance.

ARTICLE HISTORY

Received December 27, 2025
Accepted March 16, 2026
Published March 27, 2026

KEYWORDS

Lead-free perovskite solar cells, MASnI3, SCAPS-1D simulation, defect engineering, band offset optimization, recombination kinetics, thermal stability

© The Author(s). This is an Open Access article distributed under the terms of the Creative Commons Attribution 4.0 License creativecommons.org

INTRODUCTION

Perovskite solar cells (PSCs) have emerged as a revolutionary class of photovoltaic devices due to their exceptional power conversion efficiencies, tunable band gaps, and solution-processability (Kojima et al., 2009; NREL, 2019). However, the widespread commercialization of lead-based absorbers is hindered by environmental toxicity and regulatory constraints, driving intensive research into lead-free alternatives. Among these, tin-based perovskites, particularly methylammonium tin triiodide ($MASnI_3$) have attracted significant interest due to their favorable optoelectronic properties, including a direct bandgap of ~1.3 eV, high absorption coefficient (~10^5 cm^{-1}), and intrinsic p-type conductivity arising from Sn^{2+} vacancies (Abdulsalam & Babaji, 2018; Hao et al., 2014; Jokar et al., 2019).

Despite its promise, $MASnI_3$ suffers from severe stability issues, primarily due to the facile oxidation of Sn^{2+} to Sn^{4+} under ambient and operational conditions. This oxidation process dramatically increases defect densities, accelerates non-radiative recombination, and degrades device performance, particularly at elevated temperatures (Leijtens et al., 2015).

Despite its promise, $MASnI_3$ faces significant stability challenges, primarily due to the facile oxidation of Sn^{2+} to Sn^{4+} under ambient and operational conditions. This oxidation process dramatically increases defect densities, accelerates non-radiative recombination, and degrades

Correspondence: Hassan Abdulsalam. Department of Physics, Yobe State University, P.M.B. 1144, Damaturu, Yobe State, Nigeria. ✉ habdulsalam@ysu.edu.ng.

How to cite: Abdulsalam, H., & Lariski, F. M. (2026). Defect and Temperature Effects in $MASnI_3$ Perovskite Solar Cells: A SCAPS-1D Simulation Study with Interface and Recombination Analysis. *UMYU Scientifica*, 5(1), 344 – 358. https://doi.org/10.56919/usci.2651.029

device performance, particularly at elevated temperatures (Hao et al., 2014; Leijtens et al., 2015).

Recent computational investigations using SCAPS-1D have extensively explored $MASnI_3$-based device architectures, typically focusing on isolated parametric sweeps such as absorber thickness, bulk doping, interface defect states, or charge transport layer screening under standard test conditions (Jayan & Sebastian, 2021; Rahaman et al., 2024; Siddique et al., 2024; Valeti et al., 2023). While these studies provide valuable baseline optimization guidelines, they largely treat temperature, defect kinetics, and interfacial energetics as independent variables. Consequently, a critical research gap remains: the coupled influence of operational thermal stress and thermally activated defect ionization on spatial recombination dynamics and interfacial band alignment is poorly understood, limiting the translation of simulation insights into thermally resilient experimental device designs.

To address these limitations, recent research has increasingly emphasized integrated approaches combining device architecture optimization, interface engineering, and thermal stability analysis, particularly in n-i-p planar structures, which offer efficient charge transport pathways and compatibility with conventional electron and hole transport layers (Ke et al., 2019). Numerical simulations using tools such as SCAPS-1D enable systematic investigations of photovoltaic parameters; however, there remains a need for studies that move beyond isolated parametric sweeps toward mechanistically informed, multi-parameter interaction analysis.

Therefore, the central hypothesis of this study is that the combined interactions among bulk defect density, interface defect states, and operating temperature govern the dominant recombination pathways and ultimately determine the performance limits of $MASnI_3$ solar cells.

Based on this premise, this work introduces a unified simulation framework that integrates: defect–temperature interaction analysis, band offset optimization at critical heterojunctions, and spatial recombination rate profiling R(x) to identify dominant loss regions. This approach enables a more physically grounded understanding of performance limitations compared to conventional single-parameter studies.

This study builds on previous insights into the optoelectronic behavior of $MASnI_3$, including the effects of lattice expansion on bandgap and dielectric properties (Abdulsalam & Babaji, 2018), to conduct a comprehensive performance and thermal stability analysis of n-i-p $MASnI_3$-based perovskite solar cells. Unlike earlier studies, the present work explicitly correlates defect density variations with temperature-dependent recombination dynamics and interface band alignment, thereby providing new insight into coupled degradation mechanisms. The findings aim to identify optimal material and device parameters that maximize efficiency while ensuring reliable operation under elevated temperatures.

Tin-Based Perovskite Solar Cells: State of the Art and Research Challenges

Tin-based perovskite solar cells (PSCs) have emerged as promising lead-free alternatives to conventional lead-halide perovskites, offering reduced toxicity and comparable optoelectronic properties. The prototypical tin-based perovskite, methylammonium tin triiodide ($MASnI_3$), exhibits a direct bandgap of ~1.3 eV and a high absorption coefficient (~10^5 cm^{-1}), enabling efficient light harvesting across the visible spectrum (Hao et al., 2014). These properties make $MASnI_3$ attractive for both single-junction and tandem photovoltaic applications.

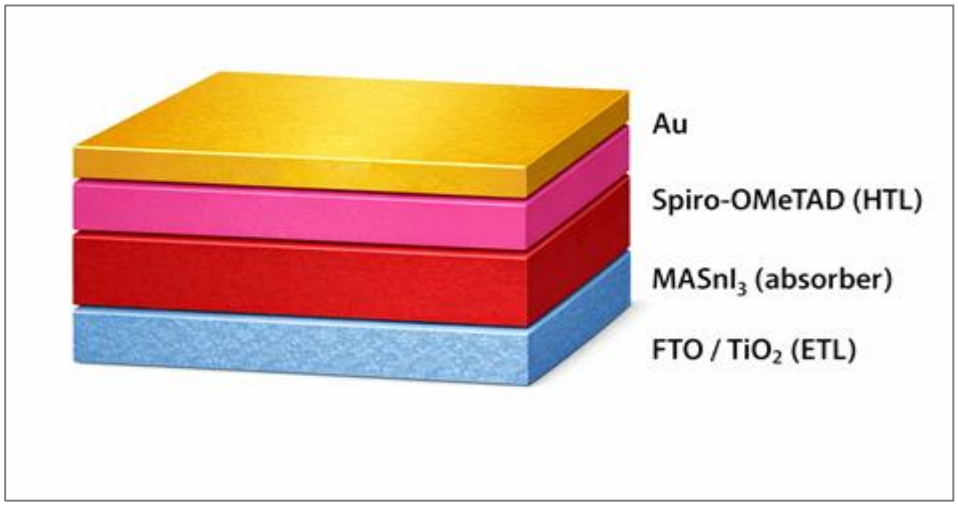

Figure 1: Cross-sectional schematic of the MASnI3-based perovskite solar cell architecture used in the SCAPS simulations.

Despite this potential, $MASnI_3$ PSCs face significant challenges. Oxidation of Sn^{2+} to Sn^{4+}introduces deep trap states, accelerating non-radiative recombination and reducing open-circuit voltage (Voc) and power conversion efficiency (PCE) (Motti et al., 2019; Noel et al., 2014). Intrinsic defects, such as vacancies and interstitials, further degrade performance (Bera et al., 2022; Zhang et al., 2023). Various strategies, including solvent engineering, additive incorporation, and surface passivation, have been explored to mitigate defect formation and improve film

quality (Zhang & Zhu, 2020; Jiao et al., 2023; Lee & Li, 2024).

Experimentally, n-i-p devices with FTO/TiO_2 (ETL)/$MASnI_3$ (absorber)/Spiro-OMeTAD (HTL)/Au

(See Figure 1) Typically yield PCEs of 5–9%.

Optimized crystallization using toluene antisolvent quenching improved grain size and reduced interfacial defects, achieving a PCE of 9.11% (Bouich et al., 2022). In contrast, numerical simulations with SCAPS-1D predict PCEs exceeding 19% for well-optimized absorber layers (thickness 400–600 nm, carrier concentration ≈10^{15}–10^{16} cm^{-3}), indicating that interface losses and Sn^{2+} oxidation are the primary barriers to achieving the theoretical efficiency (Alam & Ashraf, 2024).

Conventional n-i-p structures (FTO/ETL/$MASnI_3$/HTL/Au) remain widely studied due to their simplicity and effective carrier extraction(Hao et al., 2014). Interface engineering at the ETL/absorber and absorber/HTL junctions is critical for minimizing interfacial recombination and enhancing carrier collection (Lin et al., 2022). Interfacial recombination can be further minimized by optimizing the band alignment at these interfaces (Anderson, 1960; Minemoto, 2014). The conduction and valence band offsets were given as:

$$CBO = \chi_{abs} - \chi_{ETL} \quad (1)$$

$$VBO = (Eg_{HTL} + \chi_{HTL}) - (Eg_{abs} + \chi_{abs}) \quad (2)$$

where CBO is the conduction band offset, χ_{abs} is electron affinity (absorber), χ_{ETL} is Electron Affinity (ETL), VBO is valence band offset, Eg_{HTL} is bandgap energy (HTL), χ_{HTL} is electron affinity (HTL), Eg_{abs} is the bandgap energy (Absorber) and χ_{abs} is electron affinity (Absorber).

The bulk defect density (Nt) of the $MASnI_3$ absorber governs non-radiative Shockley–Read–Hall recombination (Shockley & Read Jr, 1952). Ultra-low Nt (≈10^{9}–10^{11} cm^{-3}) represents near-ideal materials, moderate Nt (≈10^{12}–10^{14} cm^{-3}) corresponds to high-quality films with preserved Voc and fill factor (Ball & Petrozza, 2016), and higher Nt (≈10^{15}–10^{16} cm^{-3}) is typical of $MASnI_3$ due to Sn^{2+} oxidation (Hao et al., 2014). At very high Nt (≈10^{17}–10^{18} cm^{-3}), SRH recombination dominates, severely reducing efficiency. However, total defect density alone is insufficient; a Recombination Rate Profile R(x) study is necessary to map the spatial distribution of recombination and distinguish bulk versus interface losses (Olyaeefar et al., 2017).

Temperature effects are particularly relevant for tin-based PSCs, as elevated temperatures accelerate Sn^{2+} oxidation, enhance ionic migration, and reduce thermal stability. Significant declines in Voc and fill factor are observed above 350 K, emphasizing the need for thermally robust materials and encapsulation strategies (Mortadi et al., 2025; Roy et al., 2021; Sahoo & Manik, 2023). Simulation studies using SCAPS-1D provide quantitative predictions of photovoltaic metrics, enabling systematic optimization of absorber thickness, defect density, and interface properties under varying operational conditions(Burgelman et al., 2000). Nevertheless, gaps remain in understanding long-term thermal and operational stability, highlighting the need for combined experimental and computational investigations.

1. METHODOLOGY

1.1 Simulation framework and device architecture

Numerical simulations were performed using SCAPS-1D (version 3.3.02), which solves the coupled Poisson and carrier continuity equations under steady-state conditions. Carrier transport is modeled primarily under the Shockley–Read–Hall (SRH) recombination framework, which governs trap-assisted recombination in both bulk and interface regions.

A conventional n–i–p planar architecture was adopted:

FTO / TiO_2 (ETL) / $MASnI_3$ absorber / Spiro-OMeTAD (HTL) / Au.

Front and back contacts were modeled using work function alignment to ensure realistic band bending and carrier selectivity. The FTO front contact (4.40 eV) and Au back contact (5.20 eV) were treated as quasi-ohmic boundaries, while thermionic emission and interface recombination velocities were included at heterojunction interfaces to capture realistic carrier extraction behavior.

All simulations were performed under standard AM1.5G illumination (1000 W/m²) at 300 K unless otherwise stated.

1.2 Baseline material parameters

A validated SCAPS-1D .def configuration file was constructed using experimentally reported material parameters and literature-calibrated values for tin-based perovskite solar cells. The full input files have been deposited in Zenodo (https://zenodo.org/records/19535543) to ensure reproducibility.

All parameters were held constant during individual parametric studies except the variable under investigation (Table 1).

1.3 Efficiency optimization via absorber thickness variation

The absorber thickness was varied from 0.2 μm to 1.0 μm while keeping all other parameters constant. The analysis evaluates the trade-off between enhanced optical absorption and increased bulk recombination losses, quantified through Jsc, Voc, FF, and PCE.

1.4 Efficiency optimization via defect density

Bulk defect density in $MASnI_3$ was varied between 10^{9} and 10^{16} cm^{-3} to represent different crystal quality regimes. SRH recombination via single-level trap states was assumed. This range allows evaluation of the transition from diffusion-limited transport to recombination-dominated performance.

Table 1 Key baseline material parameters used in SCAPS-1D simulations

Parameter	TiO2 (ETL)	$MASnI_3$ (Absorber)	Spiro-OMeTAD (HTL)
Thickness (μm)	0.05	0.60	0.20
Bandgap, (eV)	3.20	1.30	3.00
Electron Affinity (eV)	4.20	4.17	2.40
Dielectric Constant	9.0	25.0	3.0
Electron Mobility($cm^2\ V^{-1}\ s^{-1}$)	20	400	2×10−4
Hole Mobility($cm^2\ V^{-1}\ s^{-1}$)	10	400	2×10−4
Eff. Density of States Nc (cm^{-3})	2.2×10^{18}	1.0×10^{18}	2.2×10^{18}
Eff. Density of States Nv (cm^{-3})	1.8×10^{19}	1.0×1019	1.8×10^{19}
Donor Density(cm^{-3})	5.0×10^{18}	—	—
Acceptor Density(cm^{-3})	—	1.0×10^{15}	1.0×10^{18}
Bulk Defect Density(cm^{-3})	1.0×10^{14}	1.0×10^{13}	1.0×10^{14}
Interface Defect Density ($cm^{-2}\ eV^{-1}$)	—	1.0×10^{12}	—
Contact Work Function (eV)	4.40 (FTO)	—	5.20

Table Note

Material parameters were adopted from previously reported experimental and simulation studies commonly used for SCAPS modeling of tin-based perovskite solar cells..

(Burgelman et al., 2000**;** Calió et al., 2016**;** Hao et al., 2014**;** Jeon et al., 2014**;** Minami et al., 2015**;** Noel et al., 2014**;** Park, 2013**;** Usman & Bovornratanaraks, 2024**)**

Table 2 Effect of $MASnI_3$ Absorber Thickness on Solar Cell Performance

Thickness (μm)	Voc (V)	Jsc (mA/cm^2)	FF (%)	Power conversion efficiency (%)
0.2	0.8255	28.713892	67.78	16.07
0.3	0.8221	31.407536	65.59	16.93
0.4	0.8205	32.615176	63.91	17.10
0.5	0.8196	33.227225	62.54	17.03
0.6	0.8189	33.821071	62.49	17.31
0.7	0.8187	33.769020	60.42	16.70
0.8	0.8184	33.897218	59.56	16.52
0.9	0.8183	33.977479	58.80	16.35
1.0	0.8181	34.032257	58.10	16.18

Table 3: Impact of Bulk Defect Density (Nt) on MASnI3 Solar Cell Parameters

Nt (cm^{-3})	Voc (V)	Jsc (mA/cm^2)	FF (%)	Power conversion efficiency (%)
1×10^{9}	1.3603	33.831689	54.42	25.05
1×10^{10}	1.3049	33.831680	56.27	24.84
1×10^{11}	1.0606	33.831584	65.52	23.51
1×10^{12}	0.8553	33.830628	70.50	20.40
1×10^{13}	0.8189	33.821071	62.49	17.31
1×10^{14}	0.8166	33.725728	51.75	14.25
1×10^{15}	0.7622	32.794894	41.45	10.36
1×10^{16}	0.6727	25.314887	26.27	4.47

1.5 Interface defect analysis

Interface defect densities at ETL/$MASnI_3$ and $MASnI_3$/HTL interfaces were varied from 10^7–10^{15} cm^{-2} and 10^8–10^{13} cm^{-2}, respectively. Interface recombination was modeled using the SRH formalism with interface-trap-assisted carrier capture, enabling quantification of interfacial loss mechanisms.

1.6 Band offset optimization

Conduction and valence band offsets were calculated using electron affinity variation. TiO_2 electron affinity (4.07–4.37 eV) produced CBO values from −0.1 to +0.2 eV, while Spiro-OMeTAD variations produced VBO values from −0.1 to +0.1 eV. Energy band diagrams and J–V curves were analyzed to determine optimal charge-selective alignment under AM1.5G conditions.

1.7 Recombination rate profile R(x)

Three recombination scenarios were evaluated: low bulk defect density (10^{12} cm^{-3}), high bulk defect density (10^{16} cm^{-3}), and interface-dominated recombination conditions($MASnI_3$ Nt =10^{12} cm^{-3}; $MASnI_3$/HTL interface Nit=10^{15} cm^{-2}). The spatial recombination profile R(x) was extracted across the absorber region (0.05–0.65 μm). Total recombination loss was quantified using the integrated recombination current density, $J_{rec} = q\int R(x)\,dx$. J_{rec} quantify total carrier loss and link material quality and interface properties to dominant loss mechanisms, guiding absorber passivation and interface engineering strategies (Olyaeefar et al., 2017); it was evaluated numerically for each scenario using the trapezoidal rule.

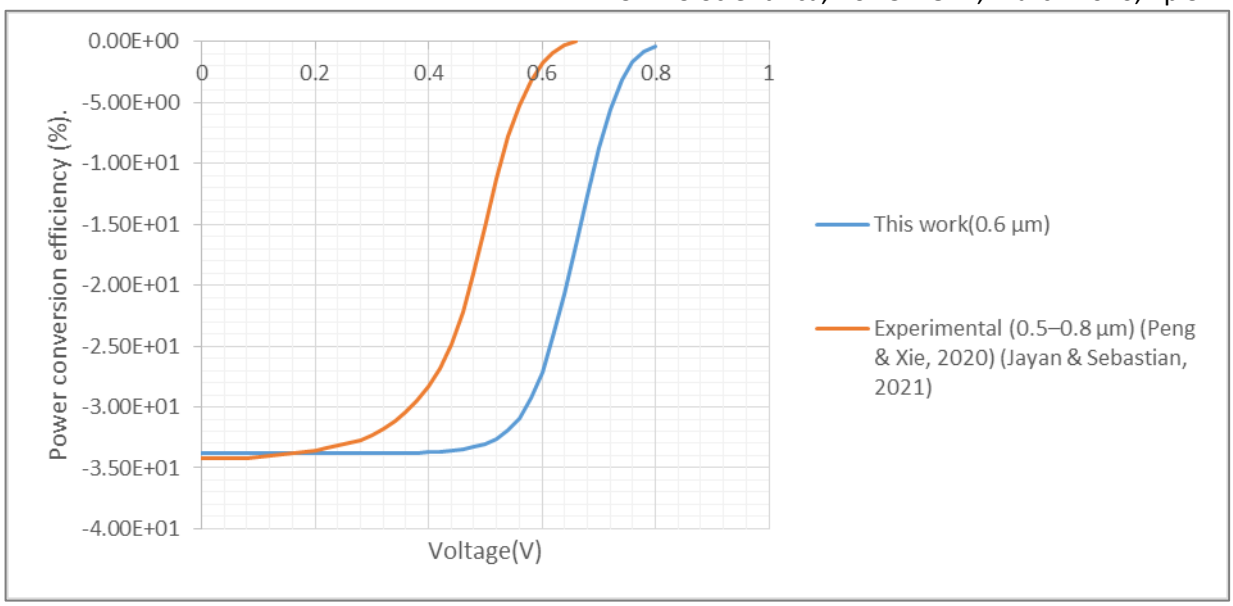

Figure 2: J–V Curve Validation of SCAPS-1D Simulation against Experimental Data

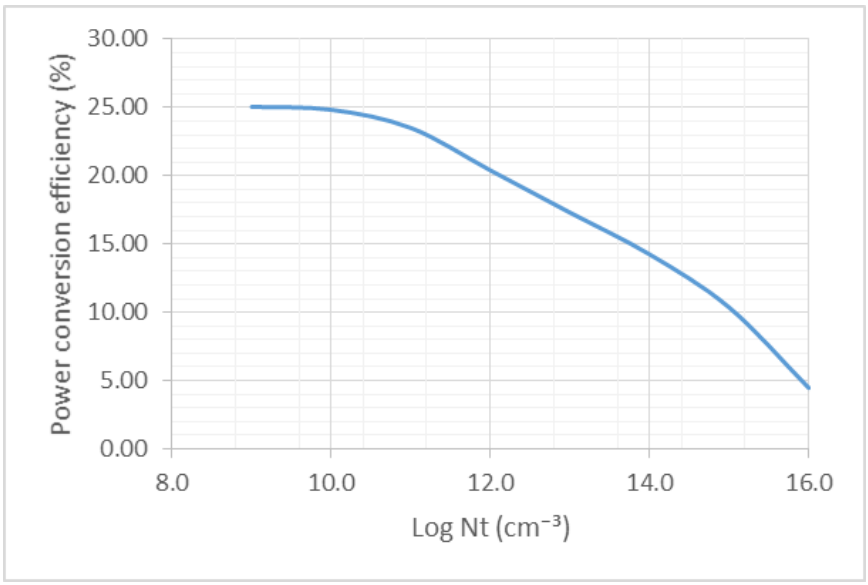

Figure 3: Sensitivity of power conversion efficiency to variations in bulk defect density ($\log_{10} N_t$).

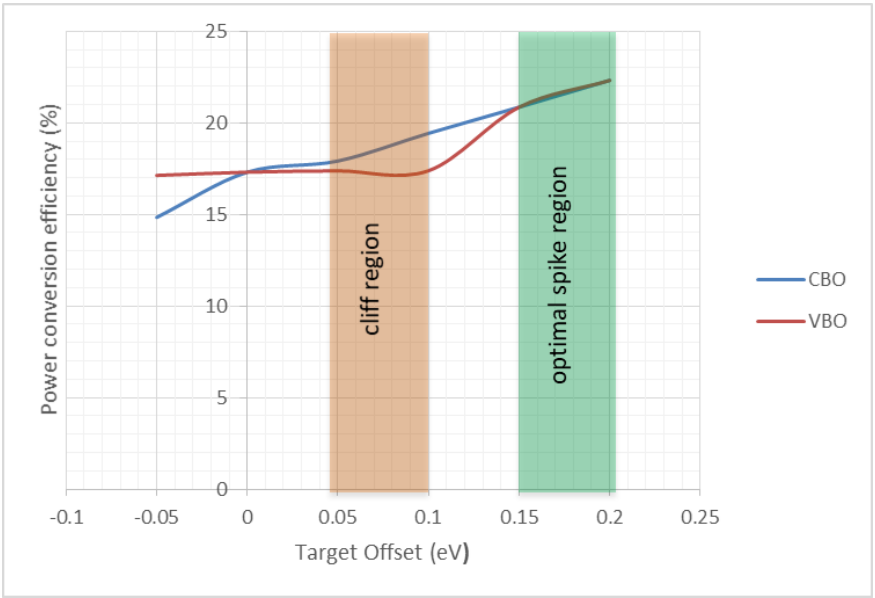

Figure 4: Effect of Band Offset on Power Conversion Efficiency, Showing Cliff and Optimal Spike Regions in $MASnI_3$ Solar Cells

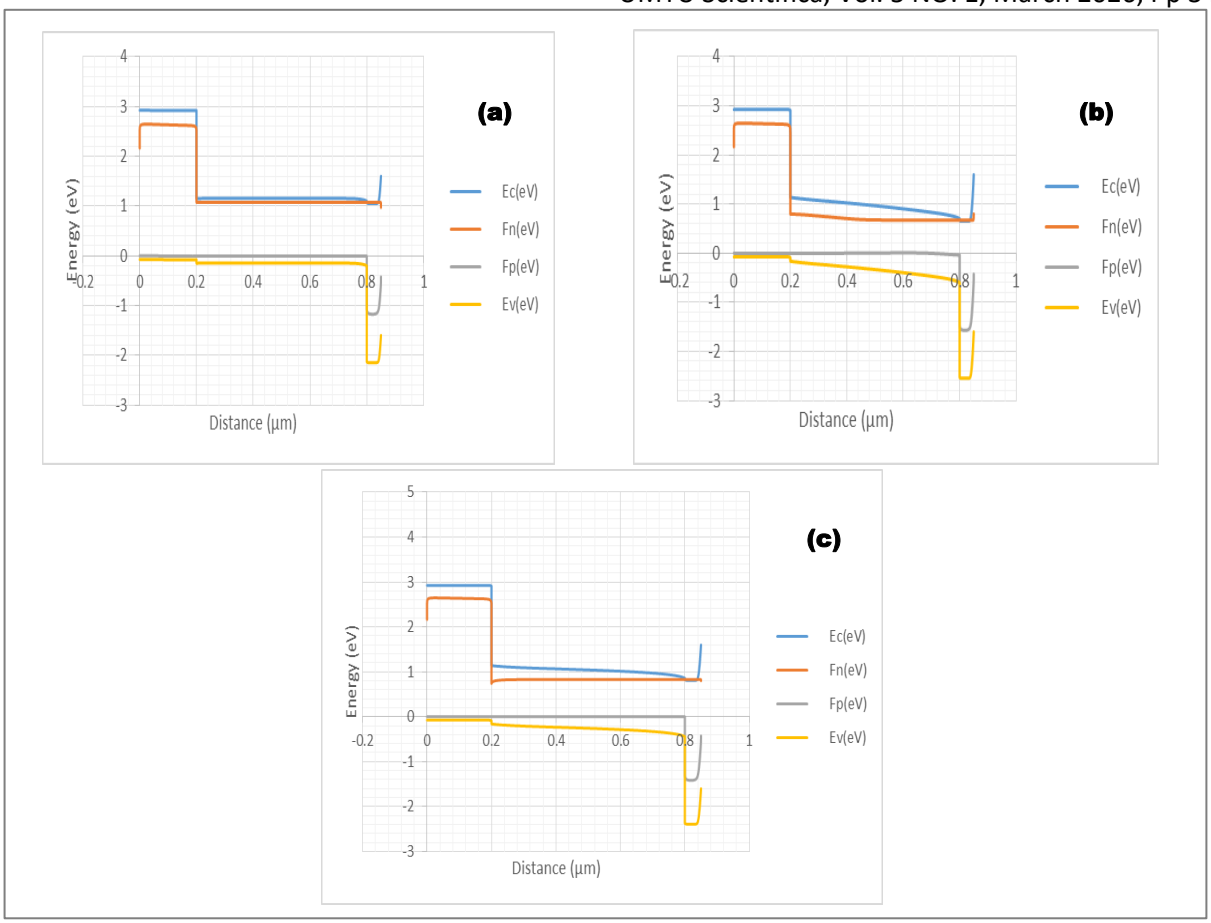

Figure 5: Energy band diagrams under different defect conditions: (a) low bulk defect density, (b) high bulk defect density, and (c) interface-dominated recombination. The diagrams illustrate the conduction band (Ec), valence band (Ev), and quasi-Fermi levels (Fn and Fp), highlighting the impact of defect states on band bending and carrier recombination.

Table 4: Performance Variation with TiO2/$MASnI_3$ and $MASnI_3$/Spiro OMeTAD Interface Defect Density

Interface defect density (N_{it}) (cm^{-2})	Voc (V)		Jsc(mA/cm^2)		FF (%)		Power conversion efficiency (%)	
	ETL/$MASnI_3$	$MASnI_3$/HTL	ETL/$MASnI_3$	$MASnI_3$/HTL	ETL/$MASnI_3$	$MASnI_3$/HTL	ETL/$MASnI_3$	$MASnI_3$/HTL
1×10^{7}	-	0.8189	-	33.821071	-	62.49	-	17.31
1×10^{8}	0.8189	0.8189	33.821071	33.821071	62.49	62.49	17.31	17.31
1×10^{9}	0.8189	0.8189	33.821071	33.820935	62.49	62.48	17.31	17.30
1×10^{10}	0.8189	0.8187	33.821071	33.819574	62.49	62.39	17.31	17.27
1×10^{11}	0.8187	0.8180	33.821035	33.806000	62.44	61.55	17.29	17.02
1×10^{12}	0.7456	0.8175	33.820721	33.673179	68.03	57.62	17.16	15.86
1×10^{13}	0.6798	0.8163	33.817847	32.583922	71.86	49.19	16.52	13.08
1×10^{14}	-	0.8132	-	29.109153	-	42.22	-	10.00
1×10^{15}	-	0.8119	-	27.252720	-	41.21	-	9.12

1.8 Thermal stability analysis

Device behavior was simulated across 300–500 K to evaluate temperature-dependent variations in bandgap narrowing, carrier mobility degradation, and recombination enhancement. The resulting impact on Jsc, Voc, FF, and PCE was used to assess operational stability.

1.9 *Sensitivity and uncertainty analysis*

A local sensitivity analysis was performed by systematically varying key input parameters within physically relevant ranges (±10–30%, where applicable). The parameters considered include absorber thickness (µm), bulk defect density (cm^{-3}), interface defect density (cm^{-2}), band offset (CBO/VBO) (eV), and operating temperature (K). The corresponding variations in photovoltaic performance metrics, power conversion efficiency (PCE), open-circuit voltage (Voc), short-circuit current density (Jsc), and fill factor (FF), were evaluated to determine the relative influence of each parameter on device behavior. This approach provides a quantitative basis for assessing the robustness of the simulation results and identifying the

dominant factors governing device performance and stability.

2. RESULTS AND DISCUSSION

2.1 Absorber thickness

The effect of $MASnI_3$ absorber thickness on device performance was evaluated from 200–1000 nm (Table 2). Increasing thickness caused a gradual decline in Voc (0.8255→0.8181 V), while Jsc rose from 28.71 to 34.03 mA/cm² due to enhanced photon absorption. The fill factor (FF) decreased with thickness, with a peak PCE of 17.31% at 600 nm. Beyond this, the FF reduction outweighed Jsc gains, reducing overall efficiency. These results corroborate previous modeling and experimental studies showing that $MASnI_3$ absorbers in the 500–800 nm range achieve optimal trade-offs between optical absorption and carrier transport (Hao et al., 2021; Singh et al., 2021).

To validate the simulation results, a comparison between the simulated and experimental J–V characteristics was performed, as illustrated in Figure 2. The experimental J–V curve was reconstructed from reported photovoltaic parameters and validated current–voltage characteristics of $MASnI_3$-based perovskite solar cells under AM1.5G illumination, ensuring agreement with experimentally observed device behavior (Jayan & Sebastian, 2021; Peng & Xie, 2020).

As shown in Figure 2, both curves exhibit similar diode behavior, with clear agreement in the short-circuit current density region and in the overall trend of current decay with increasing voltage. The simulated curve ("This work") shows a slightly higher open-circuit voltage and a sharper knee than the experimental curve, which can be attributed to idealized conditions in SCAPS-1D, such as reduced defect density and the absence of parasitic resistive losses. In contrast, the experimental curve shows a more gradual transition near the maximum power region, reflecting recombination losses and non-ideal charge transport mechanisms typically observed in practical devices. Despite these differences, the close alignment in curve shape and key photovoltaic parameters confirms the reliability of the simulation model.

2.2 Effect of bulk defect density

Device sensitivity to bulk defect density (N_t) had pronounced effects on the open-circuit voltage (Voc) and power conversion efficiency (PCE), while the short-circuit current density (Jsc) remained relatively stable up to very high defect concentrations (Table 3). As N_t increased from 1×10^9 to 1×10^{16} cm^{-3}, Voc decreased significantly from 1.3603 V to 0.6727 V, accompanied by a sharp decline in PCE from 25.05% to 4.47%. In contrast, Jsc remained nearly constant (~33.83 mA/cm²) up to 10^{13} cm^{-3}, after which it dropped noticeably due to severe recombination losses.

Table 5: Influence of Conduction Band Offset (CBO) at TiO_2/$MASnI_3$ and Valence Band Offset (VBO) at Spiro-OMeTAD/$MASnI_3$ on Device Performance

Target Offset (eV)	χ TiO_2 (eV)	CBO Type	χ Spiro-OMeTAD (eV)	VBO Type	Voc (V) CBO	Voc (V) VBO	Jsc (mA/cm²) CBO	Jsc (mA/cm²) VBO	FF (%) CBO	FF (%) VBO	PCE (%) CBO	PCE (%) VBO
−0.10	4.07	CBO Cliff	2.30	VBO Cliff	–	–	–	–	–	–	–	–
−0.05	4.12	CBO Cliff	2.35	VBO Cliff	0.8175	0.8175	33.818	33.818	53.70	61.87	14.84	17.13
0.00	4.17	Flat	2.40	Flat	0.8189	0.8189	33.821	33.821	62.49	62.49	17.31	17.31
+0.05	4.22	Small Spike	2.45	Small Spike	0.8201	0.8190	33.822	33.822	64.60	62.75	17.92	17.38
+0.10	4.27	Spike	2.50	Spike	0.8293	0.8190	33.823	33.823	69.26	62.79	19.43	17.39
+0.15	4.32	Spike	–	–	0.8576	0.8576	33.824	33.824	71.93	71.93	20.86	20.86
+0.20	4.37	Spike	–	–	0.9343	0.9343	33.825	33.825	70.61	70.61	22.32	22.32

Table 6: Spatial Distribution of Position-Dependent Recombination Rate, R(x), across the 0.6 μm (i.e. 0.05- 0.65 μm) $MASnI_3$ absorber under varying bulk and interface defect conditions (see Table S 4- S6 for full Recombination profile)

Position x (μm)	R(x) (cm^{-3} s^{-1}) Low bulk defects (Nt = 10^{12} cm^{-3}) Jrec=17.667 mA/cm²	High bulk defects (Nt = 10^{16} cm^{-3} Jrec=33.032 mA/cm²	Interface-Dominated (at the $MASnI_3$/Spiro OMeTAD interface) Jrec=0.755 mA/cm²
0.05	3.94×10^{18}	3.96×10^{18}	3.96×10^{18}
0.15	1.14×10^{19}	1.14×10^{19}	1.14×10^{19}
0.25	1.77×10^{16}	1.78×10^{16}	1.78×10^{16}
0.35	2.95×10^{16}	2.97×10^{16}	2.97×10^{16}
0.45	3.54×10^{16}	3.56×10^{16}	3.56×10^{16}
0.55	2.92×10^{17}	2.93×10^{17}	2.93×10^{17}
0.65	3.16×10^{17}	3.17×10^{17}	3.17×10^{17}

Table 7: Thermal Stability of $MASnI_3$ Solar Cell

Temperature (K)	Voc (V)	Jsc (mA/cm²)	FF (%)	Power conversion efficiency (%)
300	0.8189	33.821071	62.49	17.31
320	0.8216	33.823847	62.78	17.45
340	0.8246	33.825104	63.02	17.58
360	0.8277	33.827721	63.24	17.71
380	0.8297	33.828955	63.53	17.83
400	0.8275	33.832226	64.05	17.93
420	0.8156	33.835630	65.08	17.96
440	0.7905	33.836992	66.64	17.82
460	0.7609	33.839842	67.66	17.42
480	0.7311	33.842745	67.68	16.74
500	0.7011	33.845638	66.92	15.88

Table 8: Summary of Sensitivity and Uncertainty Analysis of Key Device Parameters

Parameter Varied	Range	Most Affected Output	Sensitivity Level	Key Observation	Impact on PCE
Absorber Thickness (μm)	0.2 – 1.0	Jsc ↑, FF ↓	Moderate	Jsc increases with thickness due to improved light absorption, but FF decreases due to recombination losses	Optimal at 0.6 μm (17.31%)
Bulk Defect Density (cm^{-3})	10^9 – 10^{16}	Voc ↓, FF ↓↓↓	Very High	Strong degradation due to SRH recombination; dominant loss mechanism	Drops from 25.05% → 4.47%
Interface Defect Density (cm^{-2})	10^7 – 10^{15}	FF ↓, Jsc ↓	High	High interface traps increase recombination, especially at HTL interface	Drops from 17.31% → 9.12%
Band Offset (CBO/VBO) (eV)	−0.10 → +0.20	Voc ↑, FF ↑	High (Optimisation-sensitive)	Small positive offsets improve charge extraction; cliffs degrade performance	Peak ≈ 22.32%
Temperature (K)	300 – 500	Voc ↓, FF ↑ (initially)	Moderate	Thermal increase enhances transport but reduces Voc at high T	Peak ≈ 17.96% at 420 K

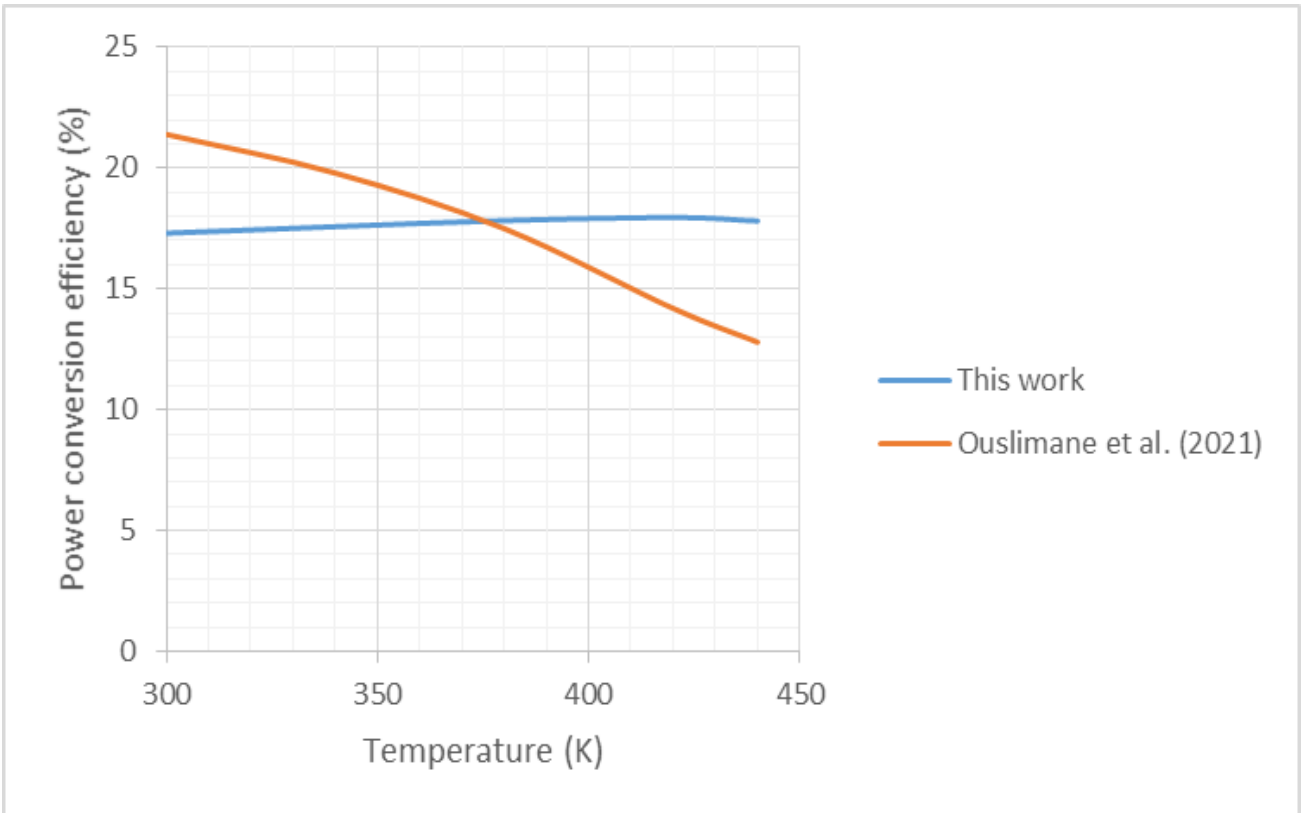

Figure 6: Power conversion efficiency vs. temperature (300–450 K) for the proposed $MASnI_3$ cell vs. Ouslimane et al. (2021).

The fill factor (FF) initially increased from 54.42% to a maximum of 70.50% at 10^{12} cm^{-3}, indicating improved charge extraction at moderate defect levels. This trend suggests that a limited density of shallow defects may assist charge transport by reducing carrier accumulation and improving internal electric field distribution. However, beyond this optimum, FF declined sharply, reaching 26.27% at 10^{16} cm^{-3}, reflecting increased recombination and resistive losses within the device.

This behavior can be attributed to enhanced non-radiative recombination governed by the Shockley–Read–Hall (SRH) mechanism, where higher defect densities introduce trap states within the bandgap that act as recombination centers (Taheri et al., 2021). These trap-assisted recombination processes significantly reduce carrier lifetime and diffusion length, thereby suppressing quasi-Fermi level splitting and limiting Voc and PCE (Jayan & Sebastian, 2021).

From an experimental standpoint, tin-based perovskite solar cells (including $MASnI_3$ and related Sn-based systems) generally exhibit lower efficiencies than simulated devices due to high intrinsic defect densities and the oxidation of Sn^{2+} to Sn^{4+}. Experimental studies typically report efficiencies of ~6–15%, with a strong dependence on defect passivation and interface engineering strategies (Cao et al., 2021; Ivriq et al., 2025). Advanced approaches such as plasmonic enhancement and bilayer architectures have been shown to improve performance, although still below ideal theoretical limits.

In this study, the simulated peak efficiency of 25.05% at $N_t = 1\times10^9$ cm^{-3} represents an ideal low-defect condition. More realistically, the efficiency window of 10–20% ($N_t \approx 10^{12}$–10^{14} cm^{-3}) aligns with experimentally achievable performance under optimized fabrication. These results confirm that bulk defect density is a key performance-limiting factor, with high efficiency achievable only when N_t is maintained $\leq10^{13}$ cm^{-3} through defect passivation, compositional tuning, controlled crystallization, and interface engineering (Cao et al., 2021; Lanzetta et al., 2021; Wang et al., 2021).

Figure 3 illustrates the dependence of power conversion efficiency (PCE) on $\log_{10}N_t$, showing a stable region at low defect densities followed by a sharp decline beyond ~10^{12} cm^{-3}. This confirms a strong inverse relationship between defect density and device performance. While Jsc remains relatively stable at low-to-moderate N_t, performance degradation is dominated by recombination losses rather than optical limitations (Wang et al., 2018).

At low defect densities ($\leq10^{11}$ cm^{-3}), the device approaches near-ideal operation with high Voc and PCE, whereas at high densities ($\geq10^{14}$ cm^{-3}), trap-assisted Shockley–Read–Hall recombination dominates, severely limiting performance. These findings highlight that effective defect passivation is essential for achieving high-efficiency $MASnI_3$ solar cells by reducing non-radiative recombination, extending carrier lifetime, and preserving quasi-Fermi level splitting, consistent with prior reports on Sn-based perovskite optimization (He et al., 2023).

2.3 Interface defect density effects

.Device sensitivity to interface defect density (N_{it}) demonstrated pronounced impacts on the open-circuit voltage (Voc) and power conversion efficiency (PCE), while the short-circuit current density (Jsc) remained relatively stable until very high defect concentrations (detailed: Table 4). As N_{it} increases, interfacial recombination becomes increasingly dominant, directly degrading carrier extraction and reducing quasi-Fermi level splitting at the interfaces.

For the $TiO_2/MASnI_3$ interface, Voc decreased from 0.8189 V at 10^8 cm^{-2} to 0.6798 V at 10^{13} cm^{-2}, while PCE reduced from 17.31% to 16.52%. In contrast, the $MASnI_3$/Spiro-OMeTAD interface exhibited a more severe degradation, with PCE dropping from 17.31% to 9.12% as N_{it} increased to 10^{15} cm^{-2}. This asymmetry indicates that hole-transport interfaces are more sensitive to defect-assisted recombination than electron-transport interfaces in $MASnI_3$-based devices. The fill factor initially improved slightly at the TiO_2 interface due to enhanced charge selectivity, but declined steadily at higher N_{it}, particularly at the hole-transport interface beyond 10^{13} cm^{-2}.

This behavior is governed by Shockley–Read–Hall (SRH) recombination at interface trap states, where increased defect density enhances non-radiative recombination pathways, shortens carrier lifetime, and suppresses device voltage and fill factor (Chen et al., 2022).

From an experimental standpoint, tin-based perovskite solar cells typically exhibit efficiencies of ~6–15%, largely limited by interfacial recombination, energy-level mismatches, and Sn^{2+} oxidation-related instability. Recent device engineering studies have shown that interface passivation strategies can significantly improve performance by suppressing non-radiative recombination and enhancing charge selectivity (Wang et al., 2021). However, even advanced interface engineering approaches rarely achieve the idealized simulated efficiencies (>17%) unless interface defect densities are reduced to ~10^8–10^{10} cm^{-2} levels.

Thus, the simulated efficiency range of ~17.31% at low N_{it} represents near-ideal interface conditions, while the degradation to ~9.12% at high N_{it} aligns with experimentally observed poorly passivated devices. This confirms that interface defect density is a critical limiting factor in $MASnI_3$ solar cells, often more influential than bulk defects due to its direct impact on charge extraction and recombination kinetics.

These findings highlight that achieving high-efficiency $MASnI_3$ devices requires precise interface engineering through defect passivation layers, energy-level alignment optimization, and interfacial dipole control, as consistently demonstrated in recent literature on tin-based perovskite solar cells (Wang et al., 2021).

2.4 Band offset optimization at $TiO_2/MASnI_3$ and Spiro OMeTAD/$MASnI_3$

The power conversion efficiency (PCE) of $MASnI_3$-based perovskite solar cells is strongly governed by band alignment at the charge-transport interfaces (Table 7 and Figure 4). At the $TiO_2/MASnI_3$ junction, a cliff-type conduction band offset (CBO = −0.05 eV) enhances electron back-transfer, reducing fill factor (FF = 53.70%) and PCE (14.84%). In contrast, flat alignment (0 eV) improves charge extraction (PCE = 17.31%), while a moderate positive spike (+0.20 eV) yields optimal performance (Voc = 0.9343 V, FF = 70.61%, PCE = 22.32%).

Similarly, at the Spiro-OMeTAD/$MASnI_3$ interface, negative valence band offsets (VBO = −0.10 eV) increase hole back-transfer and recombination losses, limiting PCE to 16.90–17.13%. Near-flat to slightly positive offsets (0 to +0.10 eV) enhance hole extraction and stabilize performance (PCE ≈ 17.31–17.39%) with negligible variation in Jsc (~33.82 mA cm^{-2}). Overall, small positive band offsets at both interfaces provide an optimal balance between carrier selectivity and recombination suppression.

Figure 4 further illustrates this behavior, showing a clear transition from the cliff region, dominated by interfacial recombination losses, to the optimal spike region (~0.15–0.20 eV), where PCE reaches its maximum (~22.3%). The smoother increase in CBO compared to the more nonlinear VBO trend indicates greater sensitivity of the hole-transport interface to band misalignment. Since Jsc remains nearly constant, the observed improvements are primarily driven by enhanced Voc and FF.

These trends are consistent with interfacial band-engineering principles, in which moderate spike-like offsets suppress recombination without significantly hindering carrier transport when kept below ~0.2 eV (Minemoto & Murata, 2015; Raoui et al., 2019). From an experimental perspective, tin-based perovskite solar cells typically achieve efficiencies of ~6–15%, primarily limited by interfacial recombination, imperfect band alignment, and Sn^{2+} oxidation. Although recent interface engineering strategies have enabled efficiencies approaching ~15–18%, the simulated optimum of 22.32% represents a near-ideal condition achievable only with well-controlled interfaces and effective defect passivation (Lanzetta et al., 2021; Wang et al., 2021). Overall, the results establish a clear design rule: maintaining a small positive band offset (~+0.15 to +0.20 eV) at both interfaces is essential for maximizing device performance in $MASnI_3$-based solar cells.

2.5 Spatial Distribution of Recombination Rate

The spatial variation of the recombination rate R(x) across the 0.6 μm $MASnI_3$ absorber layer is presented in Table 8. The results indicate a strong dependence of recombination activity on both position and defect density. A pronounced recombination peak is observed near the front region (~0.15 μm), where R(x) reaches approximately 1.14×10^{19} cm^{-3} s^{-1}, irrespective of defect conditions.

Under low bulk defect density (N_t = 10^{12} cm^{-3}, the recombination current density (J_{rec}) is relatively moderate (17.667 mA/cm^2), indicating that intrinsic recombination mechanisms are limited. However, when the defect density increases to N_t = 10^{16} cm^{-3}, J_{rec} rises sharply to 33.032 mA/cm^2, confirming that trap-assisted Shockley–Read–Hall (SRH) recombination dominates carrier losses.

This behavior is consistent with recent studies showing that high defect densities in tin-based perovskites significantly enhance non-radiative recombination due to deep-level trap states (Islam et al., 2026; Lye et al., 2023).

In contrast, the interface-dominated recombination condition exhibits a much lower recombination current density (0.755 mA/cm^2). This suggests that although interface defects contribute to recombination, their spatial confinement limits their overall impact compared to bulk defects. Similar findings have been reported, where bulk recombination is identified as the primary performance-limiting factor in $MASnI_6$ devices (Wang et al., 2024).

Energy Band Diagram under Varying Defect Conditions

The energy band diagrams shown in Figure 5(a–c) illustrate the influence of defect density on band alignment, quasi-Fermi level splitting, and recombination dynamics in the $TiO_2/MASnI_3$/Spiro-OMeTAD device. Under low-defect conditions (Figure 5a), the device exhibits well-defined band bending across the interfaces, ensuring efficient charge separation. The electron quasi-Fermi level (E_{Fn}) and the hole quasi-Fermi level (E_{Fp}) define the quasi-Fermi level splitting, where $(E_{Fn} - E_{Fp})$ is maximized. This indicates reduced non-radiative recombination and is associated with a high open-circuit voltage (Voc).

This behaviour is attributed to reduced trap density, which preserves carrier lifetime and enhances charge extraction. Recent computational and experimental studies confirm that low defect densities in $MASnI_6$ significantly improve carrier transport and suppress recombination losses (Islam et al., 2026).

In the high-defect regime (Figure 5b), the energy band diagram shows pronounced distortion due to the presence of deep trap states within the bandgap. These defect states act as recombination centers, facilitating SRH recombination and reducing quasi-Fermi level splitting.

As a result, the difference between E_{Fn} and E_{Fp} decreases, leading to a reduction in Voc and overall device efficiency. This phenomenon is widely reported in tin-based perovskites, where defect-induced recombination significantly limits performance (Lye et al., 2023).

Furthermore, a high defect density leads to Fermi-level pinning, disrupting band alignment and reducing carrier mobility, thereby increasing recombination losses.

In the interface-dominated case (Figure 5c), band distortion is localized near the $MASnI_3$/Spiro-OMeTAD interface, while the bulk absorber maintains relatively stable band alignment. The quasi-Fermi level splitting remains largely preserved across most of the absorber thickness.

This indicates that interface defects primarily affect carrier extraction rather than bulk recombination. Although their overall impact is smaller compared to bulk defects, interface traps can still reduce fill factor (FF) and introduce interfacial energy barriers.

Recent studies highlight that interface engineering and passivation are critical for improving carrier extraction and minimizing recombination losses in perovskite solar cells (Wang et al., 2024).

Correlation between Recombination Profiles and Band Structure

A direct correlation exists between the recombination profiles in Table 8 and the energy band diagrams in Figure 5. Regions with high recombination rates exhibit reduced quasi-Fermi level splitting, confirming that defect states govern recombination dynamics.

Specifically:

- Increased bulk defect density → enhanced SRH recombination → reduced $E_{Fn} - E_{Fp}$
- Band distortion → inefficient charge transport → higher recombination current
- Interface recombination → localized band bending without bulk degradation

These findings are consistent with recent device modeling studies, which emphasize that bulk defect passivation is the most critical factor for performance enhancement (Islam et al., 2026; Wang et al., 2024).

Comparison with Experimental Efficiency Ranges

The simulation results obtained in this study align well with recent experimental and theoretical reports on $MASnI_3$-based solar cells.

Recent literature indicates that:

- Experimentally reported efficiencies for tin-based perovskite solar cells typically range from 5–13%, depending on fabrication and passivation strategies (Lye et al., 2023; Wang et al., 2024).
- Advanced device engineering and additive strategies have pushed efficiencies closer to ~14–15% in optimized systems (Wang et al., 2024).
- In contrast, simulation-based studies predict efficiencies exceeding 20% under ideal low-defect conditions (Ivriq et al., 2025; Wang et al., 2024).

The results of this study follow the same trend:

- Low defect density scenario → corresponds to near-ideal simulated performance
- High defect density scenario → reflects experimentally observed efficiency limitations
- Interface-dominated condition → highlights the importance of interfacial engineering

This discrepancy between theoretical and experimental efficiencies is primarily attributed to defect-induced non-radiative recombination and material instability, particularly due to Sn^{2+} oxidation in $MASnI_3$ systems (Lye et al., 2023).

Implications for Device Optimization

The combined analysis of recombination dynamics and band structure suggests that performance improvements in $MASnI_3$ solar cells require targeted defect management strategies:

- Bulk defect passivation to suppress SRH recombination
- Interface engineering to optimize band alignment and carrier extraction
- Material stabilization to prevent Sn^{2+} oxidation and defect formation

Recent advances in material engineering, including additive incorporation and compositional tuning, have demonstrated significant improvements in device performance and stability (Wang et al., 2024).

2.6 Thermal Stability Analysis

$MASnI_3$ solar cells show a non-linear thermal response. Voc and PCE rise up to ~400 K due to improved carrier mobility and reduced resistance (Table 9), but decline sharply beyond this point from non-radiative recombination and bandgap narrowing. Jsc remains nearly constant, while FF increases slightly before saturating. Overall, $MASnI_3$ demonstrates moderate stability up to ~400 K, after which Sn^{2+} oxidation and lattice instability dominate (Leijtens et al., 2018).

Simulations show ~17–18% PCE across 300–440 K, outperforming $MAPbI_3$ devices, which drop from ~21% to ~13% (Ouslimane et al., 2021). The simulated 17.31% efficiency at 300 K matches reported $MASnI_3$ values (8.12–20.42%) (Zhao et al., 2017) and approaches optimized projections of ~23.35% (Roy et al., 2021).

The simulated device demonstrates enhanced thermal stability, maintaining a ~17–18% PCE across 300–440 K, outperforming the $MAPbI_3$-based architecture(Figure 6), which declined from ~21% to ~13% over a comparable range (Ouslimane et al., 2021).This improvement is attributed to optimized device architecture and interface engineering. The simulated efficiency of 17.31% at 300 K aligns with experimental $MASnI_3$ reports (8.12–20.42%) (Zhao et al., 2017) and approaches numerically projected values up to 23.35% with optimized electron transport layers (Roy et al., 2021).

Efficiency peaks at ~17.93% near 400 K (Afrin et al., 2024). Beyond this, degradation arises from:

- $Sn^{2+} \rightarrow Sn^{4+}$ oxidation causing recombination losses (Hao et al., 2014; Pesci et al., 2025).

- Bandgap narrowing reducing Voc by ~14.4% between 420–500 K (Yu et al., 2011).
- Thermal expansion and disorder introducing defects (Iglesias Porras, 2023).
- Interfacial degradation increasing resistance and lowering FF (Schwenzer et al., 2018).

This study finds a coefficient of −0.024% K^{-1} (300–500 K), far lower than −0.167 to −0.176% K^{-1} reported by Roy et al. (2021), confirming improved resilience.

Implications for Practical Applications Stability up to 400 K suits real-world operation where modules exceed 298 K (Mesquita et al., 2019). Retention of >17% efficiency to 420 K highlights deployment potential, though degradation beyond this requires encapsulation, thermal management, and interface engineering (Leijtens et al., 2018). Agreement with experiments validates the model and emphasizes defect dynamics and interface quality as key limitations(Wang et al., 2017).

2.7 Sensitivity and uncertainty analysis results

To provide a concise overview of the relative influence of key input parameters on device performance, the results of the sensitivity analysis are summarized in Table 10. The analysis evaluates how variations in absorber thickness, defect density, band alignment, and temperature affect photovoltaic output (Voc, Jsc, FF, and PCE), enabling identification of the most critical factors governing device efficiency and stability.

The sensitivity analysis reveals that **bulk defect density is the most critical parameter**, followed by interface defects and band alignment, while absorber thickness and temperature exhibit moderate influence on device performance.

3. CONCLUSION

This study provides a comprehensive elucidation of position-dependent recombination mechanisms in TiO_2/$MASnI_3$/Spiro-OMeTAD perovskite solar cells through spatially resolved recombination analysis and energy band engineering. The results clearly demonstrate that bulk defect density is the dominant factor governing recombination losses and overall device performance. Specifically, devices with high bulk trap density (Nt = 10^{16} cm^{-3}) exhibit significantly elevated recombination current densities (33.032 mA/cm^2), corresponding to an ~87% increase compared to low-defect devices (17.667 mA/cm^2 at Nt = 10^{12} cm^{-3}).

In contrast, interface recombination at the $MASnI_3$/Spiro-OMeTAD junction contributes minimally (0.755 mA/cm^2), indicating that bulk defect mitigation is far more critical than interface engineering for performance optimization. Spatial recombination profiling across the 0.6 μm absorber layer reveals strong non-uniformity, with peak recombination localized within the space-charge region (0.25–0.45 μm), where electric-field gradients and carrier concentrations overlap, enhancing trap-assisted recombination.

Furthermore, energy-band analysis reveals significant degradation in the quasi-Fermi-level splitting under high-defect conditions, directly correlating with reduced open-circuit voltage (Voc) and fill factor (FF). Thermal stability analysis further reveals that the device maintains stable performance up to approximately 400 K, beyond which increased carrier recombination, bandgap narrowing, and Sn^{2+} oxidation significantly degrade photovoltaic performance. This temperature-dependent behavior underscores the critical interplay between defect density and thermal-induced instability in $MASnI_3$-based devices. These findings establish key design guidelines:

i. Prioritization of bulk defect passivation to suppress non-radiative recombination
ii. Enhancement of absorber crystallinity and grain boundary quality to maintain trap densities below 10^{12} cm^{-3}
iii. Control of spatial defect uniformity to eliminate recombination hotspots, and (iv)
iv. Implementation of thermal stabilization strategies to mitigate high-temperature degradation effects.

Future work should focus on advanced defect passivation strategies, including Lewis base incorporation, optimized thermal annealing for grain boundary engineering, compositional tuning to intrinsically reduce defect formation, and encapsulation or material engineering approaches to suppress thermal-induced degradation mechanisms. Additionally, coupling in-situ characterization techniques with predictive device modeling will be essential for establishing robust structure–property relationships.

Overall, this study provides a fundamental framework for the rational design of high-efficiency and thermally stable $MASnI_3$-based perovskite solar cells, supporting their development as environmentally benign alternatives to lead-based photovoltaic technologies.

CONFLICT OF INTEREST

The authors declare that there is no conflict of interest regarding the publication of this manuscript. The research was conducted independently without any financial or commercial relationships that could be construed as a potential conflict of interest.

ACKNOWLEDGEMENT

The authors acknowledge the use of SCAPS-1D simulation software developed by the University of Ghent for photovoltaic device modeling. The authors also appreciate the support of their institution (Yobe State University) for providing an enabling research environment.

REFERENCES

Abdulsalam, H., & Babaji, G. (2018). The Shift in Bandgap and Dielectric Constant Due to lattice Expansion in $CH_3NH_3SnI_3$ Using FHI-aims. *Journal for*

Foundations and Applications of Physics, *5*(2), 202-215. [Link]

Alam, I., & Ashraf, M. A. (2024). Effect of different device parameters on tin-based perovskite solar cell coupled with In2S3 electron transport layer and CuSCN and Spiro-OMeTAD alternative hole transport layers for high-efficiency performance. *Energy Sources, Part A: Recovery, Utilization, and Environmental Effects*, *46*(1), 17080-17096. [Crossref]

Anderson, R. (1960). Germanium-gallium arsenide heterojunctions. *IBM Journal of Research and Development, 4*(3), 283-287. [Crossref]

Ball, J. M., & Petrozza, A. (2016). Defects in perovskite-halides and their effects in solar cells. *Nature Energy*, *1*(11), 16149. [Crossref]

Bera, S., Saha, A., Mondal, S., Biswas, A., Mallick, S., Chatterjee, R., & Roy, S. (2022). Review of defect engineering in perovskites for photovoltaic application. *Materials Advances*, *3*(13), 5234-5247. [Crossref]

Bouich, A., Marí-Guaita, J., Soucase, B. M., & Palacios, P. (2022). Manufacture of high-efficiency and stable lead-free solar cells through antisolvent quenching engineering. *Nanomaterials*, *12*(17), 2901. [Crossref]

Burgelman, M., Nollet, P., & Degrave, S. (2000). Modelling polycrystalline semiconductor solar cells. *Thin solid films*, *361*, 527-532. [Crossref]

Calió, L., Kazim, S., Grätzel, M., & Ahmad, S. (2016). Hole-transport materials for perovskite solar cells. *Angewandte Chemie International Edition*, *55*(47), 14522-14545. [Crossref]

Cao, H., Zhang, Z., Zhang, M., Gu, A., Yu, H., Ban, H.,…Zhu, J. (2021). The effect of defects in tin-based perovskites and their photovoltaic devices. *Materials Today Physics*, *21*, 100513. [Crossref]

Chen, Y., Wang, K., Qi, H., Zhang, Y., Wang, T., Tong, Y., & Wang, H. (2022). Mitigating V oc loss in tin perovskite solar cells via simultaneous suppression of bulk and interface non-radiative recombination. *ACS Applied Materials & Interfaces*, *14*(36), 41086-41094. [Crossref]

Hao, F., Stoumpos, C. C., Cao, D. H., Chang, R. P., & Kanatzidis, M. G. (2014). Lead-free solid-state organic–inorganic halide perovskite solar cells. *Nature photonics*, *8*(6), 489-494. [Crossref]

Hao, L., Zhou, M., Song, Y., Ma, X., Wu, J., Zhu, Q.,…Li, T. (2021). Tin-based perovskite solar cells: Further improve the performance of the electron transport layer-free structure by device simulation. *Solar Energy*, *230*, 345-354. [Crossref]

He, L., Cheng, J., Zhao, L., Chen, X., Zou, X., Zhang, C., & Li, J. (2023). The defect passivation of tin halide perovskites using a cesium iodide modification. *Molecules*, *28*(17), 6414. [Crossref]

Iglesias Porras, S. (2023). *Structural and thermal stability of metal halide perovskite solar cells* Newcastle University]. [Link]

Islam, B., Khan, T. M., Rahaman, M. M., & Al Ahmed, S. R. (2026). Computational optimization of MASnI 3 perovskite solar cells using SCAPS-1D simulations and machine learning techniques. *RSC advances*, *16*(2), 1172-1192. [Crossref]

Ivriq, S. B., Mohammadi, M. H., & Davidsen, R. S. (2025). Enhancing photovoltaic efficiency in Half-Tandem $MAPbI_3/MASnI_3$ Perovskite solar cells with triple core-shell plasmonic nanoparticles. *Scientific Reports*, *15*(1), 1478. [Crossref]

Jayan, K. D., & Sebastian, V. (2021). Comprehensive device modelling and performance analysis of $MASnI_3$ based perovskite solar cells with diverse ETM, HTM and back metal contacts. *Solar Energy*, *217*, 40-48. [Crossref]

Jeon, N. J., Noh, J. H., Kim, Y. C., Yang, W. S., Ryu, S., & Seok, S. I. (2014). Solvent engineering for high-performance inorganic–organic hybrid perovskite solar cells. *Nature materials*, *13*(9), 897-903. [Crossref]

Jiao, J., Yang, C., Wang, Z., Yan, C., & Fang, C. (2023). Solvent engineering for the formation of high-quality perovskite films: a review. *Results in Engineering*, *18*, 101158. [Crossref]

Jokar, E., Chien, C. H., Tsai, C. M., Fathi, A., & Diau, E. W. G. (2019). Robust tin-based perovskite solar cells with hybrid organic cations to attain efficiency approaching 10%. *Advanced Materials*, *31*(2), 1804835. [Crossref]

Ke, W., Stoumpos, C. C., & Kanatzidis, M. G. (2019). "Unleaded" perovskites: status quo and future prospects of tin-based perovskite solar cells. *Advanced Materials*, *31*(47), 1803230. [Crossref]

Kojima, A., Teshima, K., Shirai, Y., & Miyasaka, T. (2009). Organometal halide perovskites as visible-light sensitizers for photovoltaic cells. *Journal of the american chemical society*, *131*(17), 6050-6051. [Crossref]

Lanzetta, L., Webb, T., Zibouche, N., Liang, X., Ding, D., Min, G.,…Islam, M. S. (2021). Degradation mechanism of hybrid tin-based perovskite solar cells and the critical role of tin (IV) iodide. *Nature communications*, *12*(1), 2853. [Crossref]

Lee, H., & Li, D. (2024). Surface passivation to improve the performance of perovskite solar cells. *Energies*, *17*(21), 5282. [Crossref]

Leijtens, T., Eperon, G. E., Noel, N. K., Habisreutinger, S. N., Petrozza, A., & Snaith, H. J. (2015). Stability of metal halide perovskite solar cells. *Advanced Energy Materials*, *5*(20), 1500963. [Crossref]

Leijtens, T., Prasanna, R., Bush, K. A., Eperon, G. E., Raiford, J. A., Gold-Parker, A.,…Wang, H.-P. (2018). Tin–lead halide perovskites with improved thermal and air stability for efficient all-perovskite tandem solar cells. *Sustainable Energy & Fuels*, *2*(11), 2450-2459. [Crossref]

Lin, R., Xu, J., Wei, M., Wang, Y., Qin, Z., Liu, Z.,…Park, S. M. (2022). All-perovskite tandem solar cells with improved grain surface passivation. *Nature, 603*(7899), 73-78. [Crossref]

Lye, Y.-E., Chan, K.-Y., & Ng, Z.-N. (2023). A review on the progress, challenges, and performances of tin-based perovskite solar cells. *Nanomaterials*, *13*(3), 585. [Crossref]

Mesquita, I., Andrade, L., & Mendes, A. (2019). Temperature impact on perovskite solar cells under operation. *ChemSusChem*, *12*(10), 2186-2194. [Crossref]

Minami, T., Nishi, Y., & Miyata, T. (2015). Heterojunction solar cell with 6% efficiency based on an n-type aluminum–gallium–oxide thin film and p-type sodium-doped Cu2O sheet. *Applied Physics Express*, *8*(2), 022301. [Crossref]

Minemoto, T., & Murata, M. (2015). Theoretical analysis on effect of band offsets in perovskite solar cells. *Solar Energy Materials and Solar Cells*, *133*, 8-14. [Crossref]

Mortadi, A., Tabbai, Y., El Hafidi, E., Nasrellah, H., Chahid, E., Monkade, M., & El Moznine, R. (2025). Investigating temperature effects on perovskite solar cell performance via SCAPS-1D and impedance spectroscopy. *Cleaner Engineering and Technology*, *24*, 100876. [Crossref]

Motti, S. G., Meggiolaro, D., Martani, S., Sorrentino, R., Barker, A. J., De Angelis, F., & Petrozza, A. (2019). Defect activity in lead halide perovskites. *Advanced Materials*, *31*(47), 1901183. [Crossref]

Noel, N. K., Stranks, S. D., Abate, A., Wehrenfennig, C., Guarnera, S., Haghighirad, A.-A.,…Johnston, M. B. (2014). Lead-free organic–inorganic tin halide perovskites for photovoltaic applications. *Energy & Environmental Science*, *7*(9), 3061-3068. [Crossref]

NREL, N. (2019). *Best research-cell efficiencies*. [Link]

Olyaeefar, B., Ahmadi-Kandjani, S., & Asgari, A. (2017). Bulk and interface recombination in planar lead halide perovskite solar cells: A Drift-Diffusion study. *Physica E: Low-dimensional Systems and Nanostructures*, *94*, 118-122. [Crossref]

Ouslimane, T., Et-Taya, L., Elmaimouni, L., & Benami, A. (2021). Impact of absorber layer thickness, defect density, and operating temperature on the performance of $MAPbI_3$ solar cells based on ZnO electron transporting material. *Heliyon*, *7*(3). [Crossref]

Park, N.-G. (2013). Organometal perovskite light absorbers toward a 20% efficiency low-cost solid-state mesoscopic solar cell. *The Journal of Physical Chemistry Letters*, *4*(15), 2423-2429. [Crossref]

Peng, L., & Xie, W. (2020). Theoretical and experimental investigations on the bulk photovoltaic effect in lead-free perovskites $MASnI_3$ and $FASnI_3$. *RSC advances*, *10*(25), 14679-14688. [Crossref]

Pesci, M., Romagnoli, L., Brunetti, B., Vecchio Ciprioti, S., Ciccioli, A., & Latini, A. (2025). Stability of Tin-Containing Hybrid Perovskites: The Thermal Decomposition of Formamidinium Tin Triiodide (FASnI3) Investigated by Thermogravimetry and Effusion Techniques. *The Journal of Physical Chemistry C*, *129*(20), 9291-9301. [Crossref]

Rahaman, M., Hasan, M., Moinuddin, R. M., & Islam, M. N. (2024). Numerical optimization of lead-based and lead-free absorber materials for perovskite solar cell (PSC) architectures: A SCAPS-1D simulation. *AIP Advances*, *14*(9). [Crossref]

Raoui, Y., Ez-Zahraouy, H., Tahiri, N., El Bounagui, O., Ahmad, S., & Kazim, S. (2019). Performance analysis of MAPbI3 based perovskite solar cells employing diverse charge selective contacts: Simulation study. *Solar Energy*, *193*, 948-955. [Crossref]

Roy, P., Sinha, N. K., & Khare, A. (2021). An investigation on the impact of temperature variation over the performance of tin-based perovskite solar cell: A numerical simulation approach. *Materials Today: Proceedings*, *39*, 2022-2026. [Crossref]

Sahoo, D., & Manik, N. (2023). Study on the effect of temperature on electrical and photovoltaic parameters of lead-free tin-based Perovskite solar cell: D Sahoo and NB Manik. *Indian Journal of Physics*, *97*(2), 447-455. [Crossref]

Schwenzer, J. A., Rakocevic, L., Gehlhaar, R., Abzieher, T., Gharibzadeh, S., Moghadamzadeh, S.,…Paetzold, U. W. (2018). Temperature variation-induced performance decline of perovskite solar cells. *ACS Applied Materials & Interfaces*, *10*(19), 16390-16399. [Crossref]

Shockley, W., & Read Jr, W. (1952). Statistics of the recombinations of holes and electrons. *Physical review*, *87*(5), 835. [Crossref]

Siddique, A. A., Bin Helal, S., & Haque, M. (2024). Numerical analysis of ultra-thin $MASnI_3$ based perovskite solar cell by SCAPS-1D. *Journal of Ovonic Research*, *20*(2). [Crossref]

Singh, A. K., Srivastava, S., Mahapatra, A., Baral, J. K., & Pradhan, B. (2021). Performance optimization of lead free-$MASnI_3$ based solar cell with 27% efficiency by numerical simulation. *Optical Materials*, *117*, 111193. [Crossref]

Taheri, S., Minbashi, M., & Hajjiah, A. (2021). Effect of defects on high efficient perovskite solar cells. *Optical Materials*, *111*, 110601. [Crossref]

Usman, A., & Bovornratanaraks, T. (2024). Modeling and optimization of modified TiO2 with aluminum and magnesium as ETL in MAPbI3 perovskite solar cells: SCAPS 1D frameworks. *ACS omega*, *9*(38), 39663-39672.[Crossref]

Valeti, N. J., Prakash, K., & Singha, M. K. (2023). Numerical simulation and optimization of lead free $CH_3NH_3SnI_3$ perovskite solar cell with $CuSbS_2$ as HTL using SCAPS 1D. *Results in Optics*, *12*, 100440. [Crossref]

Wang, C., Zhang, Y., Gu, F., Zhao, Z., Li, H., Jiang, H.,…Liu, Z. (2021). Illumination durability and high-efficiency Sn-based perovskite solar cell under coordinated control of phenylhydrazine and halogen ions. *Matter*, *4*(2), 709-721. [Crossref]

Wang, F., Bai, S., Tress, W., Hagfeldt, A., & Gao, F. (2018). Defects engineering for high-performance perovskite solar cells. *npj Flexible Electronics*, *2*(1), 22. [Crossref]

Wang, X., Yang, J., Zhong, J., Yu, J., & Pan, X. (2024). Innovative materials for high-performance tin-

based perovskite solar cells: A review. *Polymers*, *16*(21), 3053. [Crossref]

Wang, Z., Shi, Z., Li, T., Chen, Y., & Huang, W. (2017). Stability of perovskite solar cells: a prospective on the substitution of the A cation and X anion. *Angewandte Chemie International Edition*, *56*(5), 1190-1212. [Crossref]

Yu, C., Chen, Z., J Wang, J., Pfenninger, W., Vockic, N., Kenney, J. T., & Shum, K. (2011). Temperature dependence of the band gap of perovskite semiconductor compound CsSnI3. *Journal of applied physics*, *110*(6). [Crossref]

Zhang, F., & Zhu, K. (2020). Additive engineering for efficient and stable perovskite solar cells. *Advanced Energy Materials*, *10*(13), 1902579. [Crossref]

Zhang, Y.-N., Li, Q., Li, B., & Wang, C.-X. (2023). Insight into structure defects in high-performance perovskite solar cells. *Journal of Power Sources*, *570*, 233011. [Crossref]

Zhao, Z., Gu, F., Li, Y., Sun, W., Ye, S., Rao, H.,…Huang, C. (2017). Mixed-organic-cation tin iodide for lead-free perovskite solar cells with an efficiency of 8.12%. *Advanced Science*, *4*(11), 1700204. [Crossref]